Computation of Transfer Maps from Surface Data

with applications to ILC Damping Ring wigglers

Chad Mitchell
University of Maryland

August 13, 2009

Abstract Summary

- Developing methods to produce accurate charged-particle transfer maps for realistic beam-line elements of accelerator devices.

- Such methods use accurate 3-d field data provided by finite element modeling (Opera) to incorporate fringe field effects, nonlinear multipoles into a map description of beam dynamics.

- Once accurate transfer maps have been found for individual beam-line elements, one can determine all single-particle properties of the machine: dynamic aperture, tunes, chromaticities, anharmonicities, linear and nonlinear lattice functions, etc.

- Key is the use of surface data to compute interior data. Surface must enclose design trajectory and lie within all iron or other sources.

Overview

I. Toward the International Linear Collider
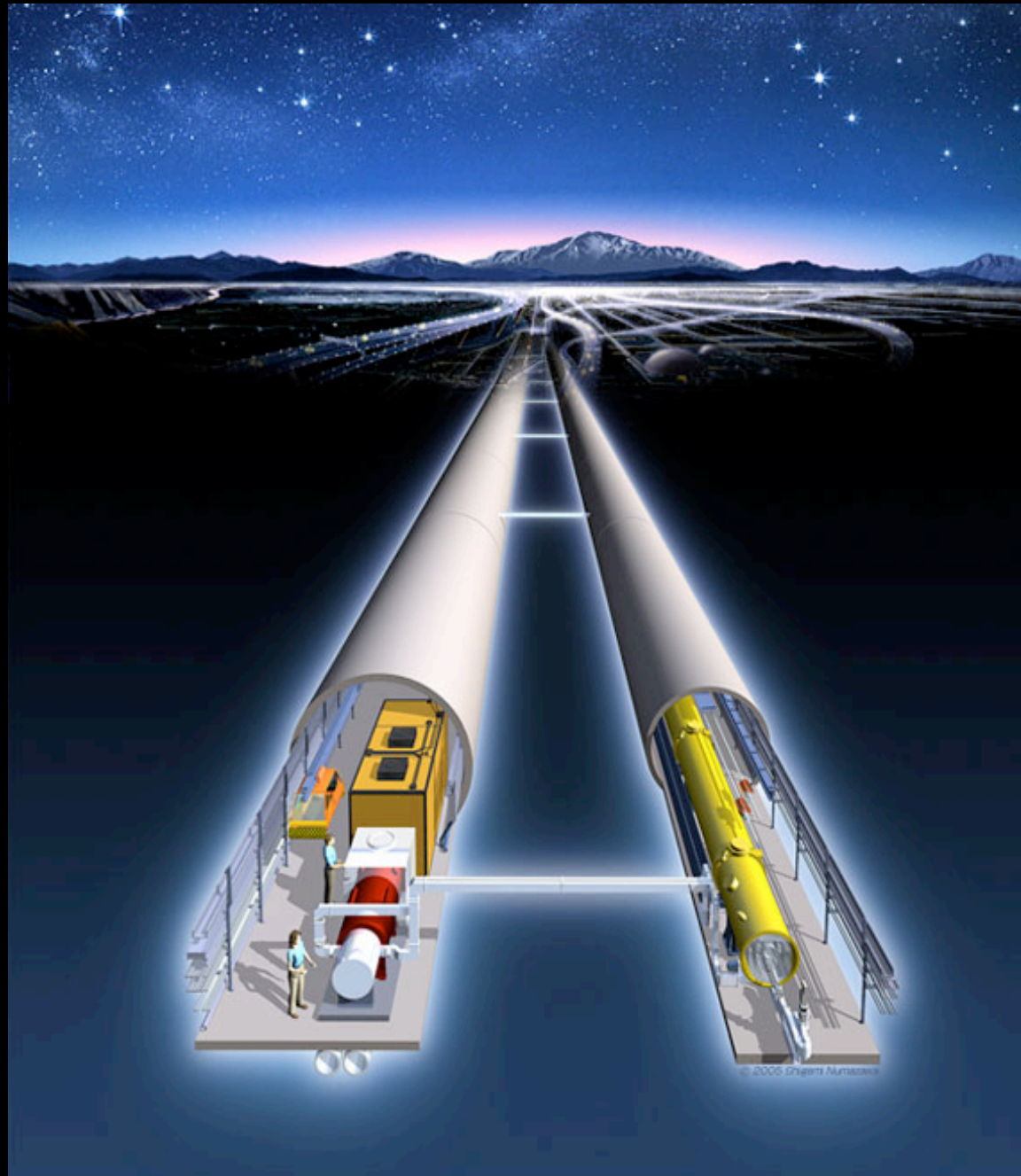
The International Linear Collider (ILC) is a proposed new 200-500 GeV linear electron-positron collider, designed with a planned upgrade to 1 TeV.
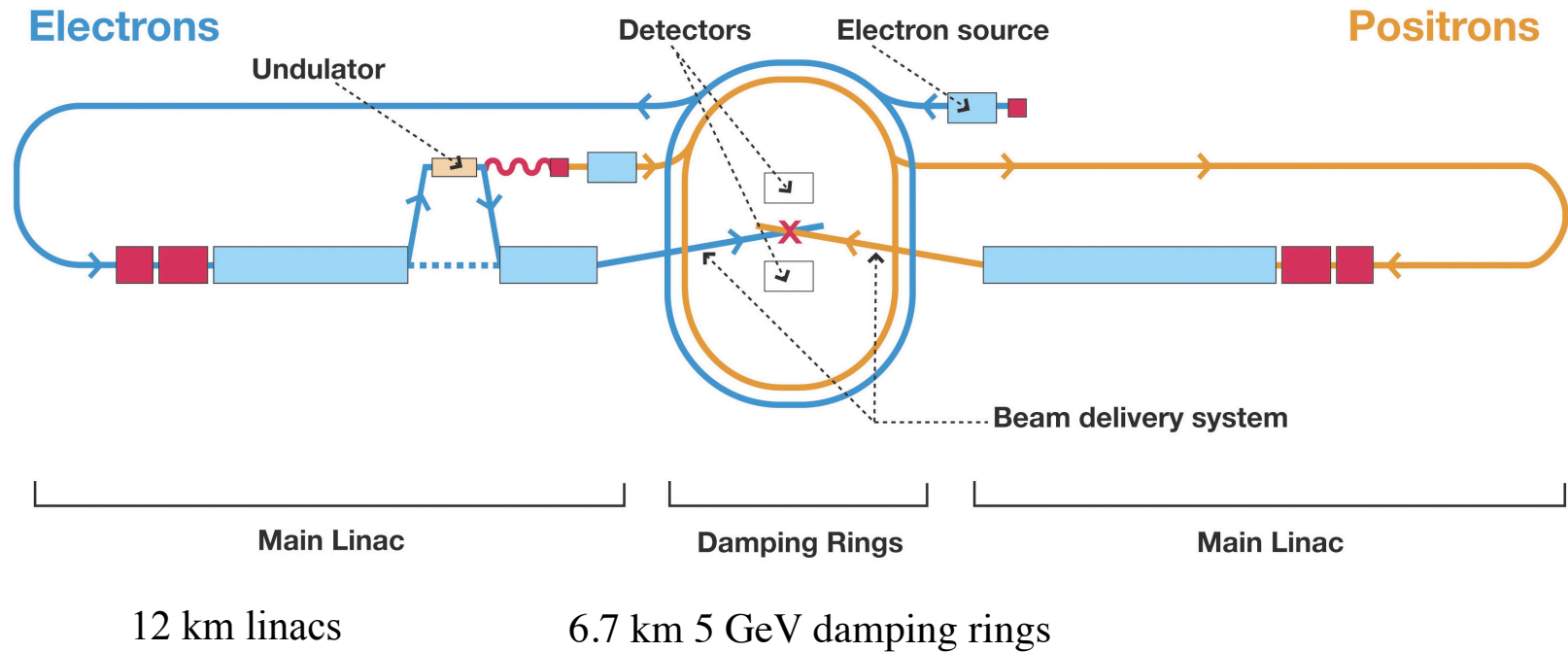
Construction projected to begin around 2015, contingent on results from the LHC and international agreement.

Purpose: Study precision physics at the Terascale in conjunction with the Large Hadron Collider (LHC) at CERN--in particular, properties of the Higgs and possible super-symmetric particles.

Possible sites:

- Near Fermilab outside Chicago, Illinois, USA

- CERN facility, Geneva, Switzerland

- One of several candidate sites in Japan

Layout of the ILC

Electrons Undulator Detectors Electron source **Positrons**

Beam delivery system

Main Linac   Damping Rings   Main Linac

12 km linacs   6.7 km 5 GeV damping rings

Driven by 1.3 GHz superconducting rf cavities with 31.5 MV/m

2×10^{10} particles per 300 μm bunch
2670 bunches per 1 ms pulse
Pulse rate of 5 Hz
Peak luminosity $2 \times 10^{34} \text{cm}^{-2}\text{s}^{-1}$

operating parameters

Design of the ILC Damping Rings

Damping rings serve to condition injected bunches from the sources into small, cleanly separated bunches for use in the main linac.

Synchrotron radiation damping is used to damp the large emittance of the injected beams (decrease phase space volume of particle beam) to values required to obtain high luminosity:

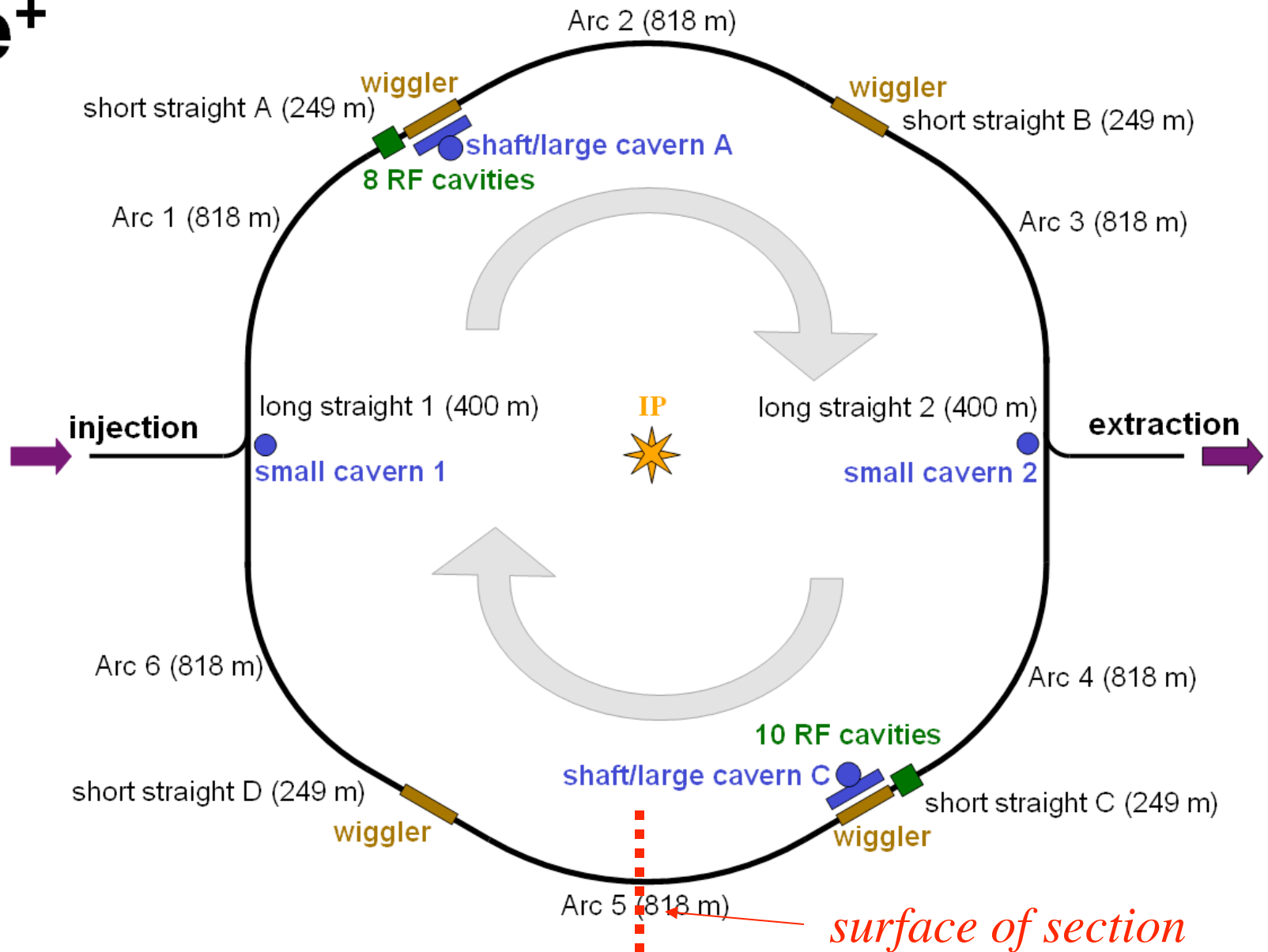$$L = \frac{f_{rep} n_b N^2}{4\pi\sigma_x\sigma_y}$$

5.7 nm x 640 nm beam spot

Damping is achieved by passing the beam through 200 m of wiggler magnets with large, oscillating vertical fields, repeatedly for ~ 10,000 turns.

Damping rings must balance many competing requirements, including:

• Small equilibrium emittance

• Short damping time

• Large acceptance (dynamic aperture)

Layout of the Damping Rings

e⁺

Arc 2 (818 m)

wiggler

short straight A (249 m)

shaft/large cavern A

8 RF cavities

wiggler

short straight B (249 m)

Arc 1 (818 m)

Arc 3 (818 m)

long straight 1 (400 m)

IP

long straight 2 (400 m)

injection

small cavern 1

extraction

small cavern 2

Arc 6 (818 m)

Arc 4 (818 m)

10 RF cavities

shaft/large cavern C

short straight D (249 m)

wiggler

short straight C (249 m)

wiggler

Arc 5 (818 m)

surface of section

II. Map Methods

Given the phase space coordinates $\mathbf{z} = (q_1, p_1, q_2, p_2, q_3, p_3)$, we represent the dynamics of a single particle in each beamline element as a mapping:

$$z^{fin} = \mathcal{M} z^{in}$$
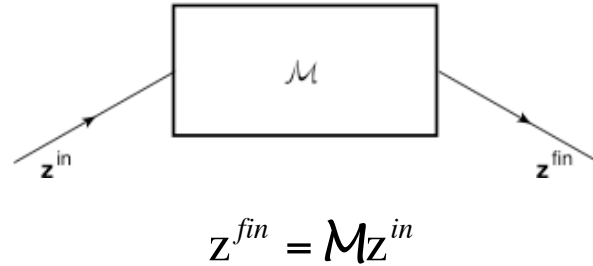
where z^{in} and z^{fin} are the initial coordinates at entry and final coordinates at exit, respectively.

Maps for adjacent beamline elements may be composed (concatenated) to obtain a single map for one full revolution around the ring.

Maps resulting from Hamiltonian motion are *symplectic*. The Jacobian matrix

$$M_{jk} = \frac{\partial z_j^{fin}}{\partial z_k^{in}} \qquad \text{must satisfy} \qquad M^T J M = J \qquad \text{where} \qquad J = \begin{pmatrix} 0 & 1 & 0 & 0 & 0 & 0 \\ -1 & 0 & 0 & 0 & 0 & 0 \\ 0 & 0 & 0 & 1 & 0 & 0 \\ 0 & 0 & -1 & 0 & 0 & 0 \\ 0 & 0 & 0 & 0 & 0 & 1 \\ 0 & 0 & 0 & 0 & -1 & 0 \end{pmatrix}$$

Lie methods for symplectic maps

Given an analytic function f, define a corresponding Lie operator $:f:$ which acts on analytic functions g such that

$$:f:g = [f,g]$$

where

$$[f,g] = \sum_{j=1}^{3}\left(\frac{\partial f}{\partial q_j}\frac{\partial g}{\partial p_j} - \frac{\partial g}{\partial q_j}\frac{\partial f}{\partial p_j}\right) \qquad \textcolor{red}{\text{Poisson bracket}}$$

Similarly, the Lie transformation generated by f is defined by the series

$$\exp(:f:) = \sum_{n=0}^{\infty}\frac{1}{n!}:f:^{n}$$

Any analytic symplectic map which also maps the origin into itself can then be written

$$\mathcal{M} = \mathcal{R}_2 e^{:f_3:}e^{:f_4:}e^{:f_5:}e^{:f_6:}\ldots$$

where $\mathcal{R}_2$ is the linear part of the map, represented by a matrix R_2, and each f_m is a homogeneous polynomial of degree m.

The Hamiltonian for charged particle motion in electric and magnetic fields is given by

$$H = \sqrt{m^2 c^4 + c^2 (\boldsymbol{p} - q\boldsymbol{A})^2} + q\phi$$

It is convenient to treat the longitudinal coordinate z as the independent variable, and to treat time and its corresponding conjugate momentum as dependent variables.

$$K = -\sqrt{\frac{(p_t + q\phi)^2}{c^2} - m^2 c^2 - (\boldsymbol{p}_\perp - q\boldsymbol{A}_\perp)^2} - qA_z$$

Map must satisfy the evolution equation $\quad \dfrac{d\mathcal{M}}{dz} = \mathcal{M} : -K :$

producing a set of differential equations for $\quad R_2$ and the coefficients of the generators f_m.

Requires expansion about the design orbit $x^d(z)$, $p_x^d(z)$, $y^d(z)$, $p_y^d(z)$ etc. through the beamline element:

$$K = \sum_{s=1}^{S} h_s(z) K_s(\delta x, \delta p_x, \delta y, \delta p_y, \delta \tau, \delta p_\tau)$$

linear map - terms of degree 2
generator f_m - terms of degree $\leq m$

III. Computing Realistic Maps

Suppose $\phi = 0$. To obtain the $h_s(z)$, we need expressions of the form:

$$A_w(x,y,z) = \sum_{l=1}^{L} a_l^w(z) P_l(\delta x, \delta y) \quad \text{with} \quad w = x,y,z$$

Field data may be available on some 3-d mesh
- measured data (3d magnetic sensors)
- electromagnetic field solvers (eg., finite-element codes)

Numerical differentiation is unreliable for high-order $a_l^w(z)$ due to amplification of noise.

Noise spectrum ~ flat to $k = \pi / h$
Introduces weight to high frequencies not present in true field B_y

$$\frac{\partial^n B_y}{\partial z^n} = F^{-1}\left[(ik)^n F[B_y] \right] \qquad \text{where} \qquad F[B_y] = \frac{1}{\sqrt{2\pi}} \int_{-\infty}^{\infty} e^{ikz} B_y(x,y,z)\, dz$$

accentuates large spatial frequencies

Surface Fitting

• Fit measured/numerical field data to the boundary surface of a domain containing the design trajectory and excluding all iron or other sources (eg., "cylinder" infinite in z with uniform cross-section).

• Interpolate inward using Maxwell's equations. In a source-free region, solutions are smooth functions.

• Obtain an analytic representation of the interior vector potential A and its Taylor coefficients $a_w^l(z)$ in terms of surface data alone.

• Highly accurate and robust against numerical errors. Errors are damped as one moves away from the surface into the interior.

error appearing in derivative of order m $\leq \left(\dfrac{3m}{d}\right)^m \max_S |\delta B|$

due to properties of harmonic functions

Advantages of Surface Fitting

- Maxwell equations are exactly satisfied.

- Error is globally controlled. The error must take all extrema on the boundary, where we have done a controlled fit.

- Careful benchmarking against analytic results for arrays of magnetic monopoles.

- Insensitivity to errors due to inverse Laplace kernel smoothing. (High frequency errors are preferentially damped, improving accuracy in high-order derivatives.) Insensitivity to noise improves with increased distance from the surface.

- Techniques can also be applied to electric and radio-frequency beamline elements.

Realistic transfer maps can now be computed for all beamline elements of any machine, e.g. the ILC damping rings, using surface methods:

- Solenoids and multipoles -- circular cylinder (M. Venturini)

- RF cavities -- circular cylinder (D. Abell)

- Wiggler magnets -- elliptical / rectangular / circular cylinder (C. Mitchell)

- Bending dipoles -- bent box / bent cylinder (C. Mitchell, P. Walstrom)

IV. Results for Various Geometries

Straight-axis geometries:
      circular cylinder
      elliptical cylinder   use known Green's function
      rectangular cylinder
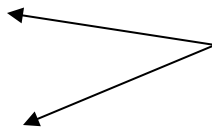
"Bent" geometries:
      use new geometry-independent integration kernels

We investigate:

• Error estimates

• Dependence of smoothing properties on domain geometry

• Numerical benchmarks

Consider the elliptical cylinder case.

Fitting ILC Wiggler Data Using Elliptical Cylinder

▪Data on regular Cartesian grid

4.8cm in x, dx=0.4cm

2.6cm in y, dy=0.2cm

480cm in z, dz=0.2cm

▪Field components B_x, B_y, B_z in one
quadrant given to a precision of 0.05 G.

fringe region

▪Place an imaginary elliptic cylinder between
pole faces, extending beyond the ends of the
magnet far enough that the field at the ends is
effectively zero.

▪Fit data onto elliptic cylindrical surface
using bicubic interpolation to obtain the
normal component on the surface.

▪Compute the interior vector potential and
all its desired derivatives from surface data.
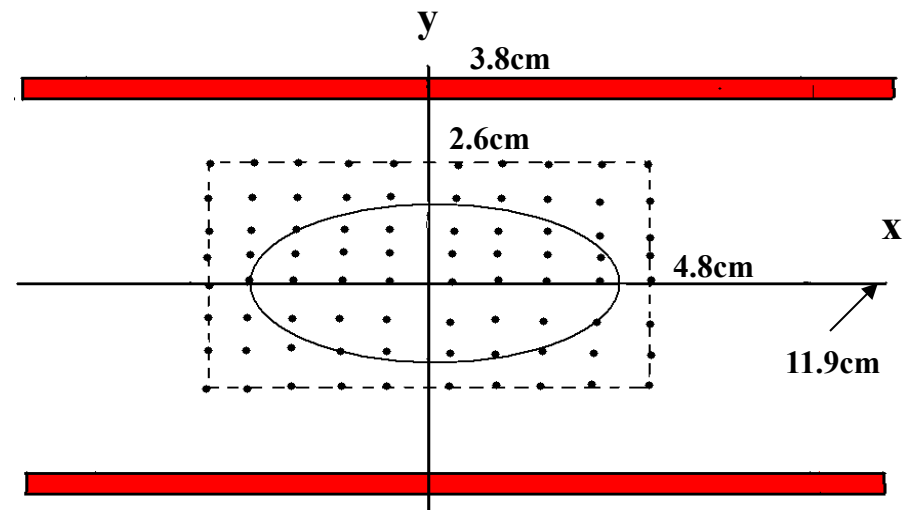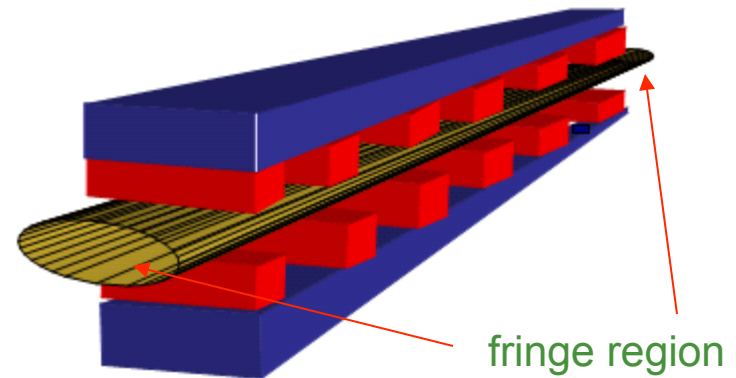
Elliptic Coordinates

Defined by relations:

$$x = f \cosh u \cos v$$
$$y = f \sinh u \sin v$$

where f=a (distance from origin to focus).

Letting z=x+iy, w=u+iv we have

$$z = \Im(w) = f \cosh w$$

Jacobian:

$$J(u,v) = \left|\Im'(w)\right|^2 = \left|f \sinh w\right|^2 = \frac{1}{2} f^2 [\cosh(2u) - \cos(2v)]$$

Laplacian:

$$\nabla^2 = \frac{1}{J(u,v)}\left(\frac{\partial^2}{\partial u^2} + \frac{\partial}{\partial v^2}\right) + \frac{\partial^2}{\partial z^2}$$
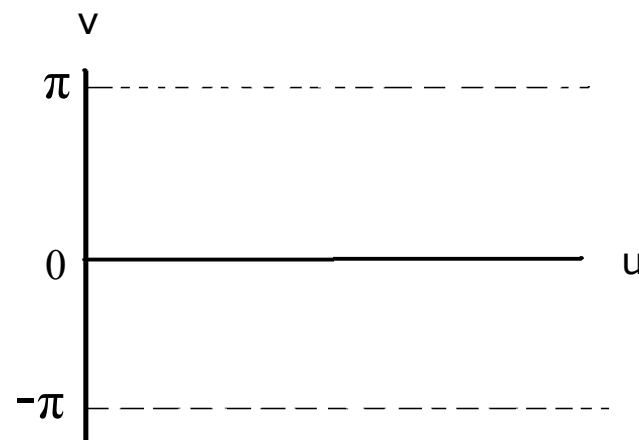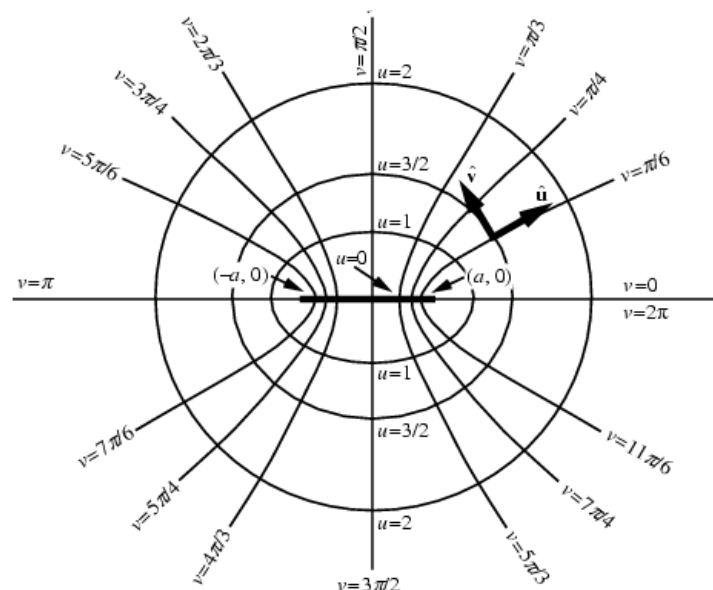
Boundary-Value Solution

- Fitting done in a source-free region, so we can use a scalar potential to write $\boldsymbol{B} = \nabla\psi$. Then $\nabla\cdot\boldsymbol{B} = 0$ gives the Laplace equation $\nabla^2\psi = 0$. Make the Fourier decomposition

$$\psi(x,y,z) = \int_{-\infty}^{\infty} dk e^{ikz}\tilde{\psi}(x,y,k) \quad ,$$

  from which it follows that $(\nabla_\perp^2 - k^2)\tilde{\psi}(x,y,k) = 0$.

- Separation of variables in elliptic coordinates gives the solution:

$$\tilde{\psi}(x,y,k) = \sum_{n=0}^{\infty}\left[\left(\frac{F_n(k)}{Se_n'(u_b,k)}\right)Se_n(u,k)se_n(v,k) + \left(\frac{G_n(k)}{Ce_n'(u_b,k)}\right)Ce_n(u,k)ce_n(v,k)\right],$$

  where u_b is the value of u on the boundary, and

$$F_m(k) = \int_0^{2\pi} dv\sqrt{J(u_b,v)}\,\tilde{B}_u(u_b,v,k)se_m(v,k)$$

$$G_m(k) = \int_0^{2\pi} dv\sqrt{J(u_b,v)}\,\tilde{B}_u(u_b,v,k)ce_m(v,k)$$

$$B_u(u_b,v,z) = \int_{-\infty}^{\infty} dk e^{ikz}\,\tilde{B}_u(u_b,v,k).$$

Power Series Expansion in x and y

Various identities involving Mathieu functions and Bessel functions enable the expansion of $\psi(x,y,z)$ as a power series in x and y with z-dependent coefficients, and corresponding power series expansions of the vector potential A in the form:

$$A_{\begin{Bmatrix}x\\y\end{Bmatrix}} = \sum_{m=1}^{\infty}\sum_{l=0}^{\infty}\frac{(-1)^l(m-1)!}{2^{2l}\,l!(l+m)!}\begin{Bmatrix}x\\y\end{Bmatrix}(x^2+y^2)^l\left[\mathrm{Re}(x+iy)^m\,C_{m,s}^{[2l+1]}(z)-\mathrm{Im}(x+iy)^m\,C_{m,c}^{[2l+1]}(z)\right]$$

$$A_z = \sum_{m=1}^{\infty}\sum_{l=0}^{\infty}\frac{(-1)^l(2l+m)(m-1)!}{2^{2l}\,l!(l+m)!}(x^2+y^2)^l\left[-\mathrm{Re}(x+iy)^m\,C_{m,s}^{[2l]}(z)+\mathrm{Im}(x+iy)^m\,C_{m,c}^{[2l]}(z)\right]$$

where

$$C_{r,s}^{[m]}(z) = \frac{1}{\sqrt{2\pi}}\frac{i^m}{2^r\,r!}\int_{-\infty}^{\infty}dk\,e^{ikz}k^{r+m}\left[\sum_{n=0}^{\infty}\frac{g_s^{2n+1}(k)B_r^{(2n+1)}(k)}{Se'_{2n+1}(u_b,k)}F_{2n+1}(k)\right]$$

$$C_{r,c}^{[m]}(z) = \frac{1}{\sqrt{2\pi}}\frac{i^m}{2^r\,r!}\int_{-\infty}^{\infty}dk\,e^{ikz}k^{r+m}\left[\sum_{n=0}^{\infty}\frac{g_c^{2n+1}(k)A_r^{(2n+1)}(k)}{Ce'_{2n+1}(u_b,k)}G_{2n+1}(k)\right].$$

- The quantities $C_{r,s}^{[m]}(z)$ and $C_{r,c}^{[m]}(z)$ are called generalized on-axis gradients. Note that

$$C_{1,s}^{[2]} = \left(\frac{d}{dz}\right)^2 C_{1,s} \text{, where } C_{1,s} = C_{1,s}^{[0]} \text{, etc.}$$

- The vertical field then takes the form:

$$B_y = C_1(z) + 3C_3(z)(x^2 - y^2) - \frac{1}{8}C_1^{[2]}(z)(x^2 + 3y^2)$$

$$+ \frac{1}{192}C_1^{[4]}(z)(x^4 + 6x^2y^2 + 5y^4) - \frac{1}{16}C_3^{[2]}(z)(3x^4 + 6x^2y^2 - 5y^4)$$

$$+ C_5(z)(5x^4 - 30x^2y^2 + 5y^4) + O(x,y)^5$$

Here, for simplicity, we have assumed that $\boldsymbol{B}$ has midplane symmetry.

- There are similar expressions for the other components of $\boldsymbol{B}$ and the components of $\boldsymbol{A}$. The coefficients $a_l^w(z)$ are proportional to the on-axis gradients.

Dipole Field Benchmark

Exactly soluble field in which all derivatives of the vector potential and on-axis gradient functions can be determined analytically.
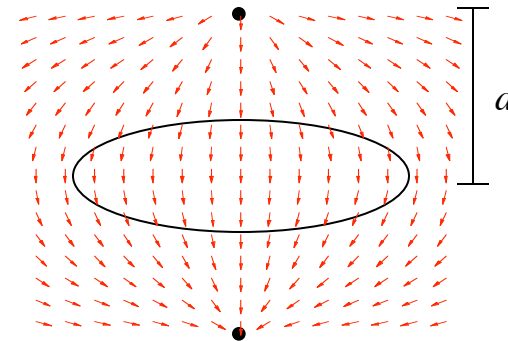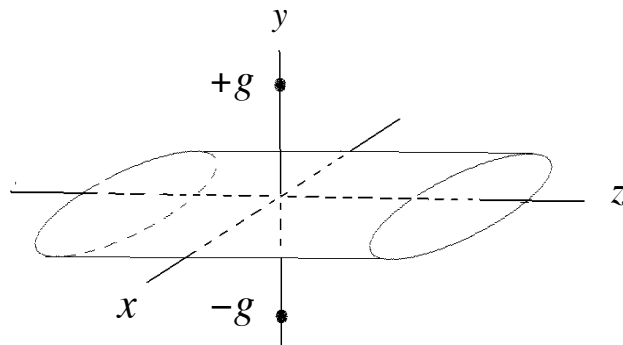

$$C_{n,s}(z) = (-1)^{(n-1)/2} \frac{g}{a^{n+1}} \frac{(2n)!}{2^{2n-2}(n!)^2} \beta^{2n+1}(z)$$

$$\beta(z) = \frac{a}{\sqrt{z^2 + a^2}}$$

• Field values are fit to the surface and used to compute on-axis gradients numerically. Tested for ellipses of two different aspect ratios: 4:3 and 5:1.

• Resulting on-axis gradients C_1, C_3, C_5, C_7 and their derivatives accurate to better than 1 part in 10^4 (error relative to peak).

• Similar benchmarks performed for circular and rectangular cylinder geometries.

Fit to the Proposed ILC Wiggler Field Using Elliptical Cylinder
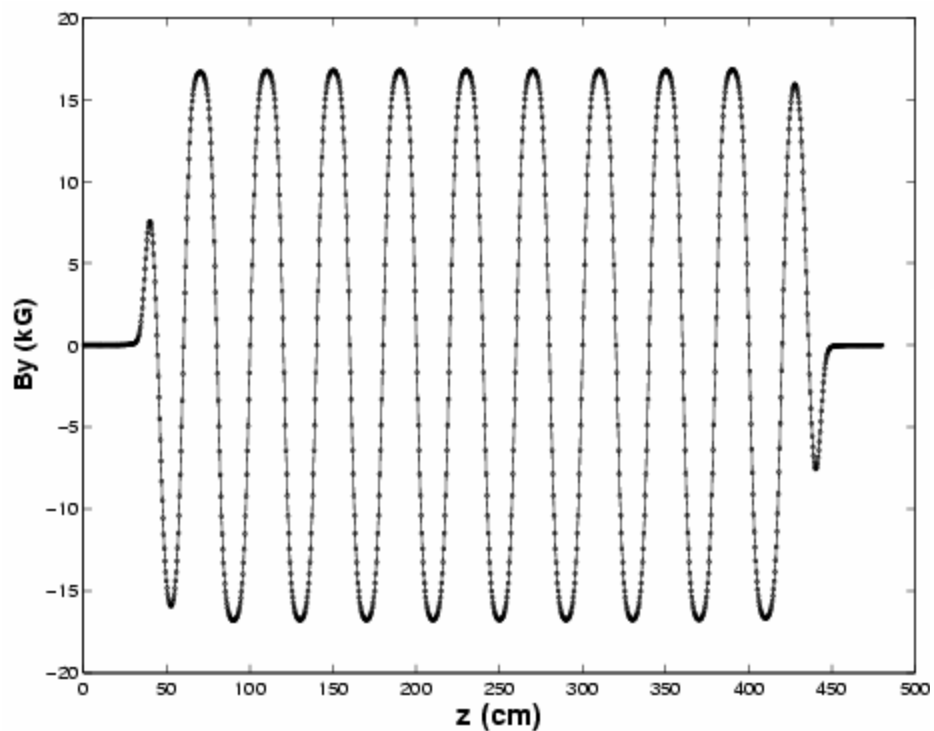
Fit to vertical field By
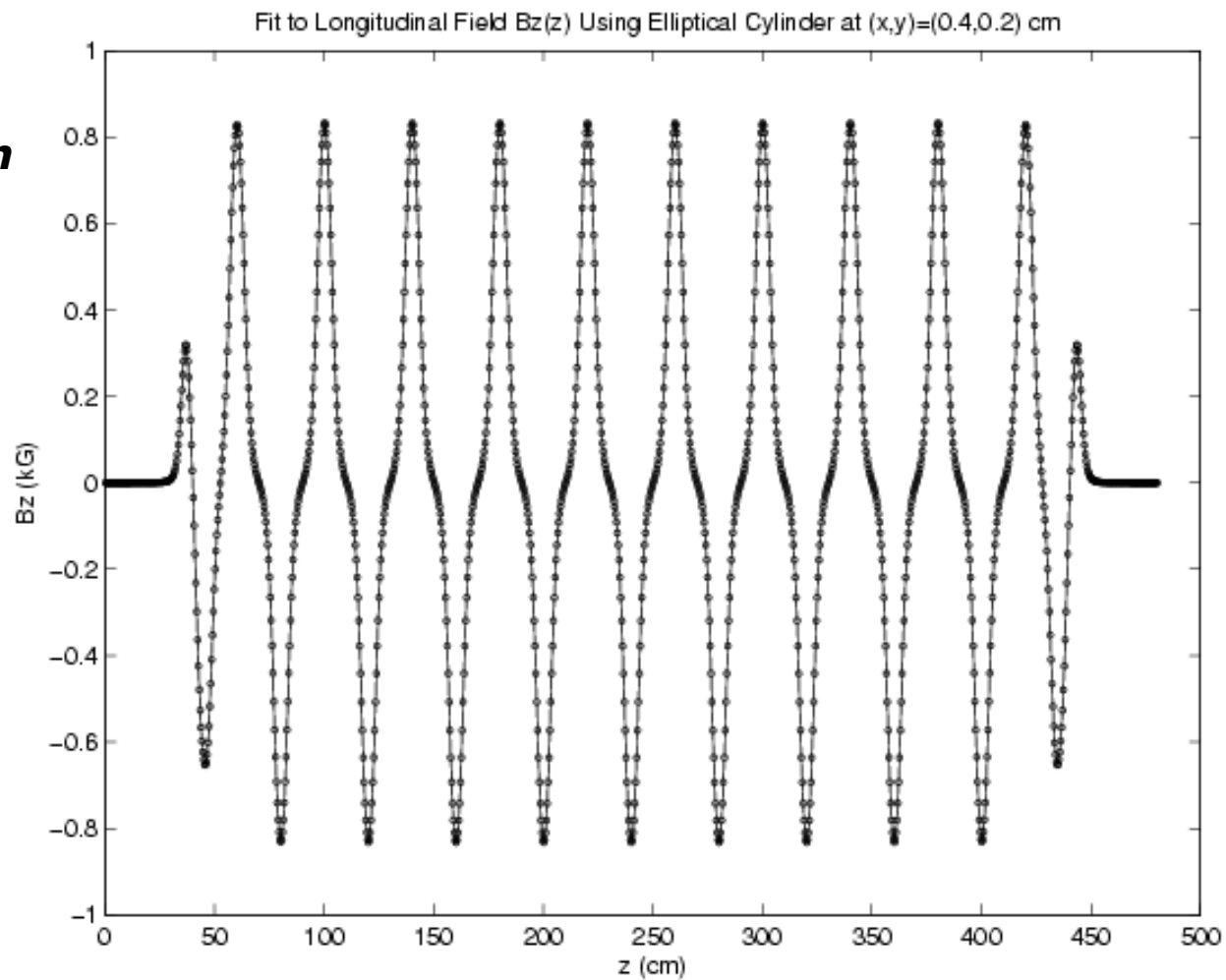at x=0.4cm, y=0.2cm.

Residuals ~ 0.5G / 17kG
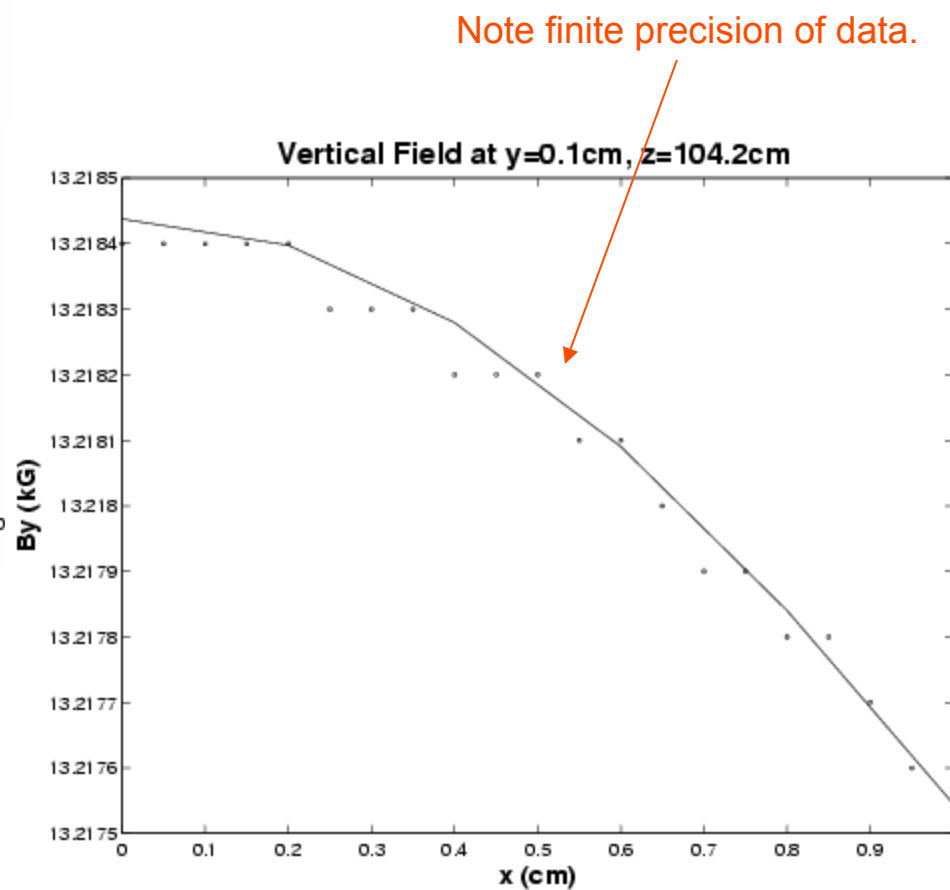
Fit to the Proposed ILC Wiggler Field Using Elliptical Cylinder

No information about Bz was used to create this plot.

Fit to longitudinal field Bz at x=0.4cm, y=0.2cm.

Fit to Longitudinal Field Bz(z) Using Elliptical Cylinder at (x,y)=(0.4,0.2) cm

Numerical Smoothing

We have seen that the generalized on-axis gradients $C_r^{[m]}(z)$ are given as the Fourier integrals of the angular Mathieu coefficients F_{2n+1} and G_{2n+1} multiplied by certain kernels (weights). For example,

$$C_{r,s}^{[m]}(z) = \frac{i^m}{\sqrt{2\pi}} \int_{-\infty}^{\infty} e^{ikz} k^m \sum_{n=0}^{\infty} \Lambda_{2n+1}^{r}(k) F_{2n+1}(k) dk \propto \int_{-\infty}^{\infty} e^{ikz} \Lambda_{1}^{r}(k) F_1(k) dk + \int_{-\infty}^{\infty} e^{ikz} \Lambda_{3}^{r}(k) F_3(k) dk + \ldots$$

•Noise in the surface values contributes weight to the high-frequency components of the angular Mathieu coefficients $F_m(k)$.

•Kernels (weights) die off quickly for large k and m, providing an effective cutoff that serves as a low-pass filter to minimize the effect of these high-frequency components on the $C_{r,s}^{[m]}$.

First 10 Integration Kernels Contributing to C_5(z) for 4:1 Ellipse
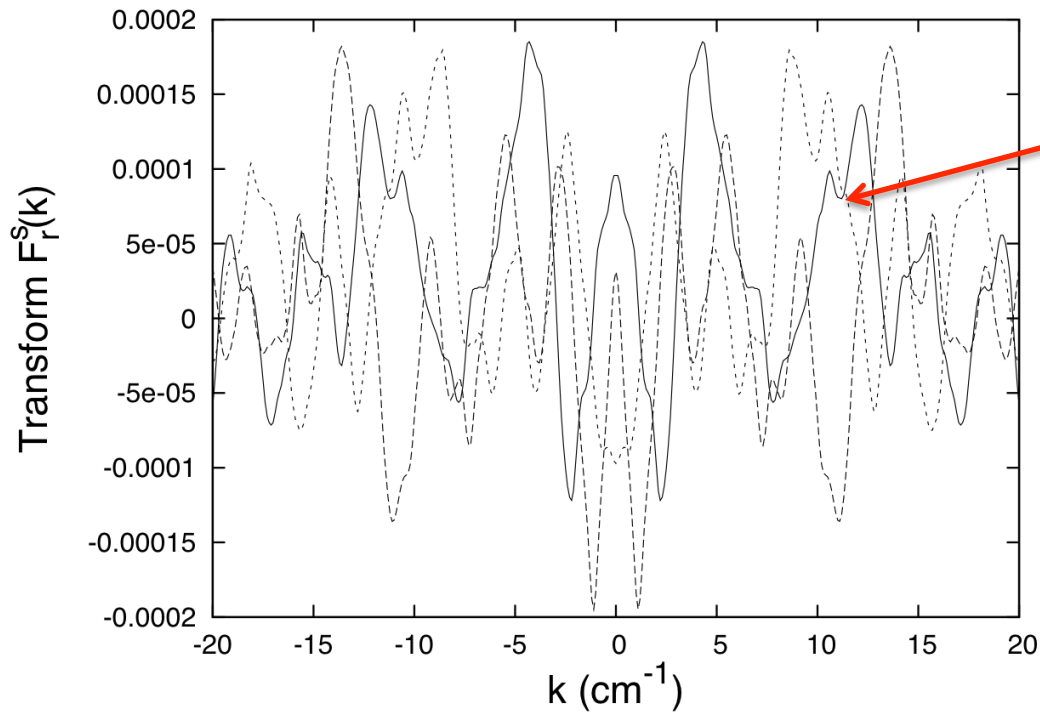
$$\Lambda_n^r \sim k^\alpha e^{-kx}$$
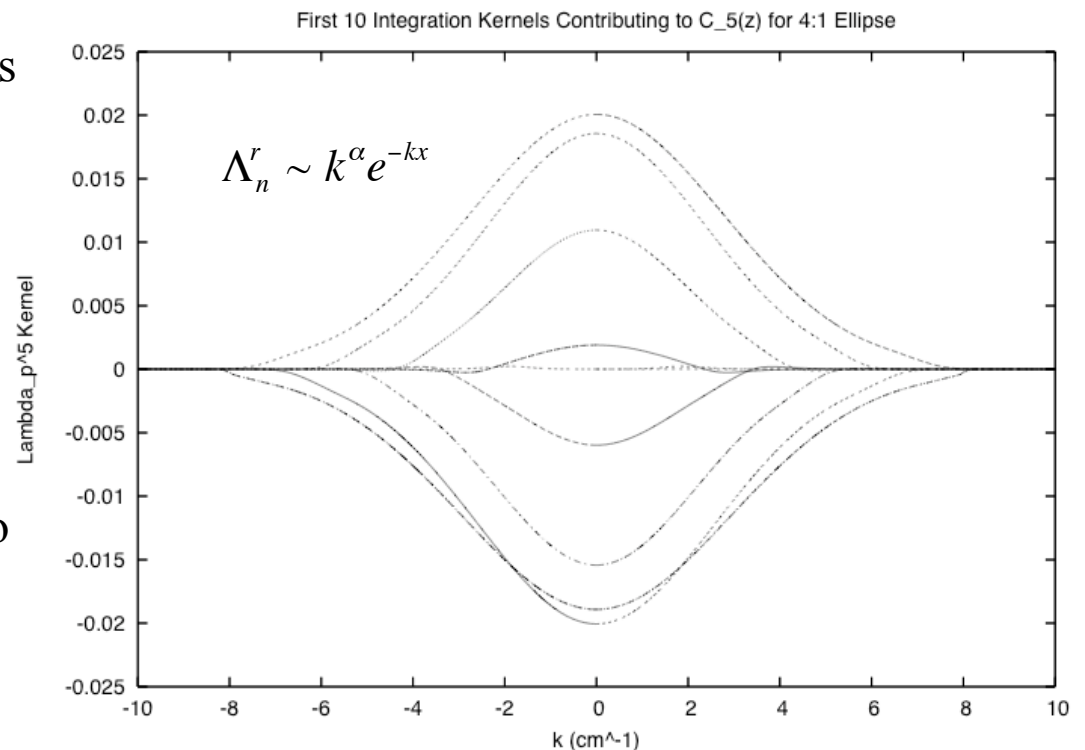
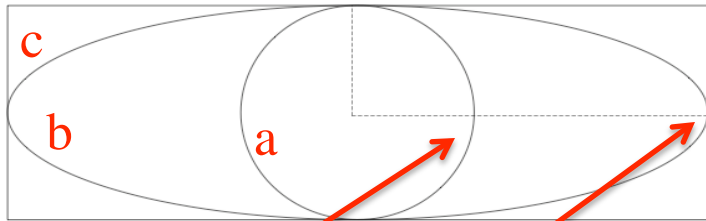For our model of noise, let $B_y(0,0,z)$ denote the on-axis monopole doublet field and

$$B_x^{noise}(x_j, y_j, z_j) = \varepsilon B_y(0,0,z_j)\delta_x(j)$$, where $\varepsilon = 0.01$ and

$$B_y^{noise}(x_j, y_j, z_j) = \varepsilon B_y(0,0,z_j)\delta_y(j)$$

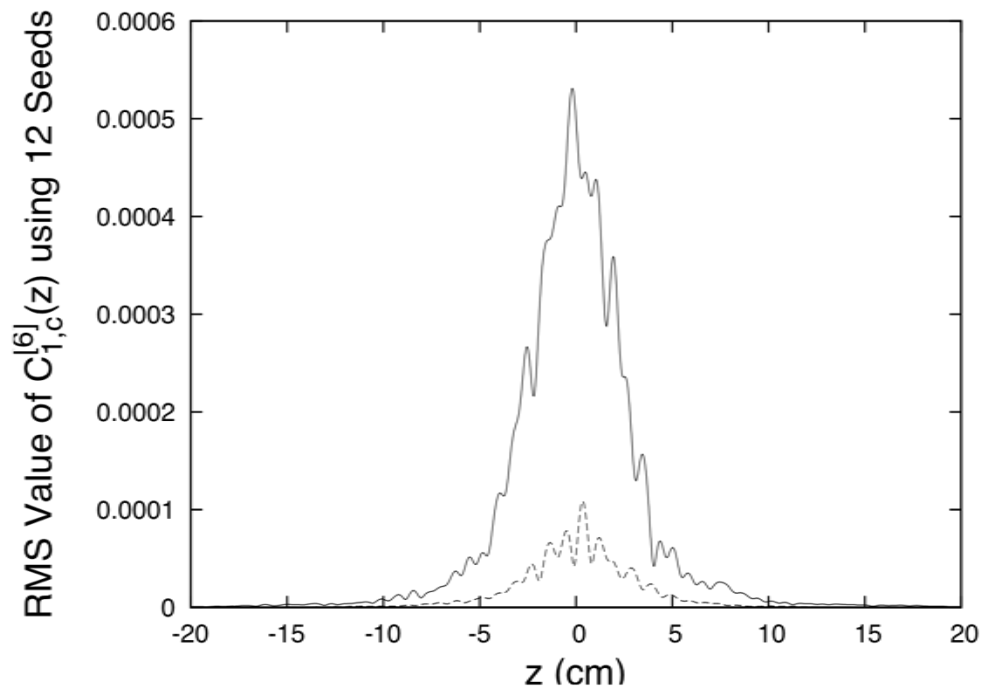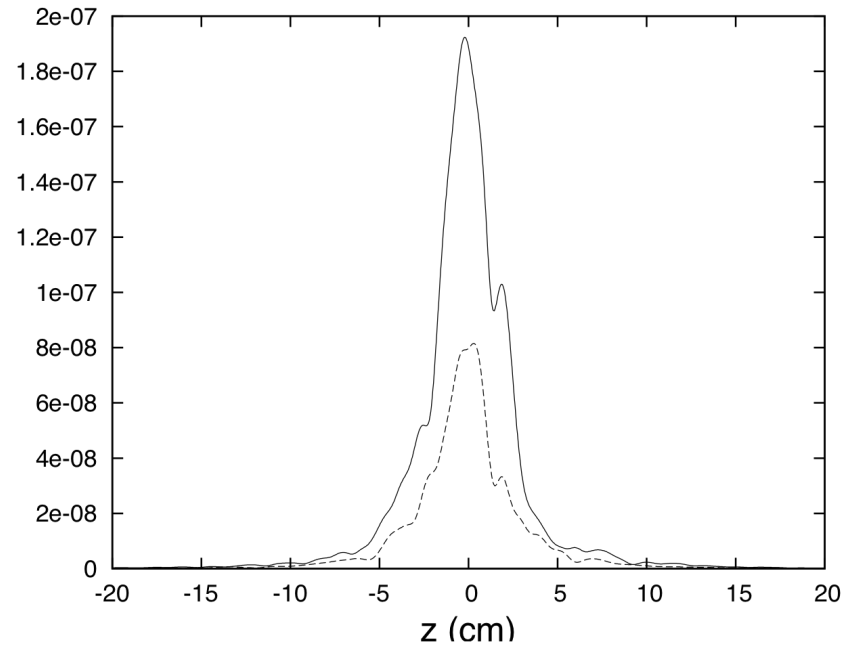$\delta_x(j), \delta_y(j)$ are uniformly distributed random variables in the interval [-1,1].

real parts of the functions $\tilde{F}_r^s(k)$ for r=1,3,5 generated by a pure noise field

c

b   a

R=2 cm; semimajor axis 4 cm

RMS Value of $C_{7,c}^{[0]}(z)$ using 12 Seeds

z (cm)

RMS Value of $C_{1,c}^{[6]}(z)$ using 12 Seeds

z (cm)

rms value of generalized gradients
produced using 12 random seeds

solid line – circular cylinder
dashed – elliptical cylinder

The Bent Box and Other Geometries

• For the straight-axis cylinder domains, only the normal component of $\boldsymbol{B}$ on the surface is used to determine interior vector potential.

• The circular, elliptical, and rectangular cylinder are special in that Laplace's equation is separable for these domains.

• For elements with significant sagitta, such as dipoles with large bending angles, we must generalize to more complicated domains in which Laplace's equation is not separable.

• Surface data for general domains can again be used to fit interior data provided both $\boldsymbol{B}_{normal}$ and ψ are available on the surface. The magnetic vector potential in the interior can be determined by the integration of surface data against a geometry-independent kernel.
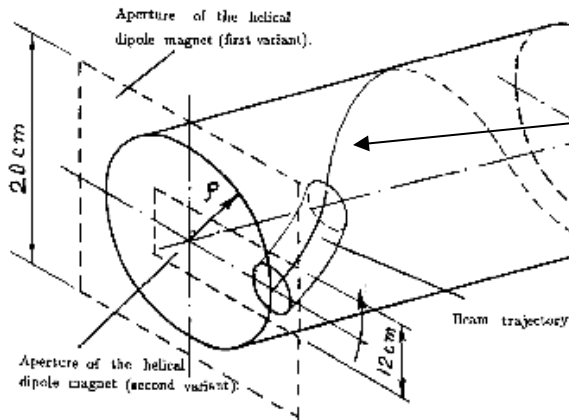
General Surfaces: Large-Sagitta Dipole
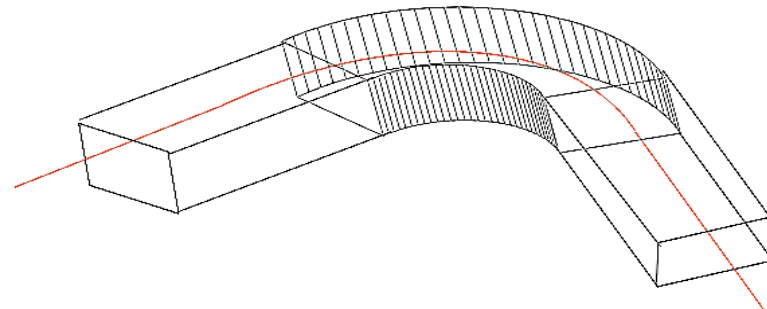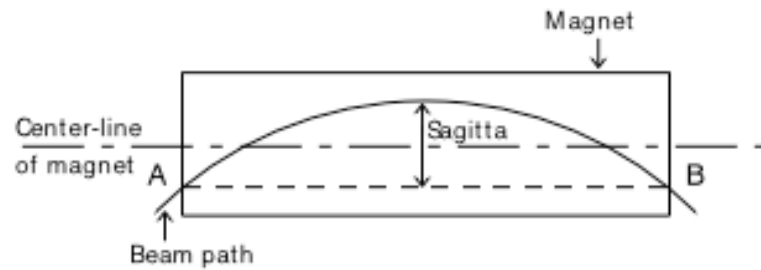
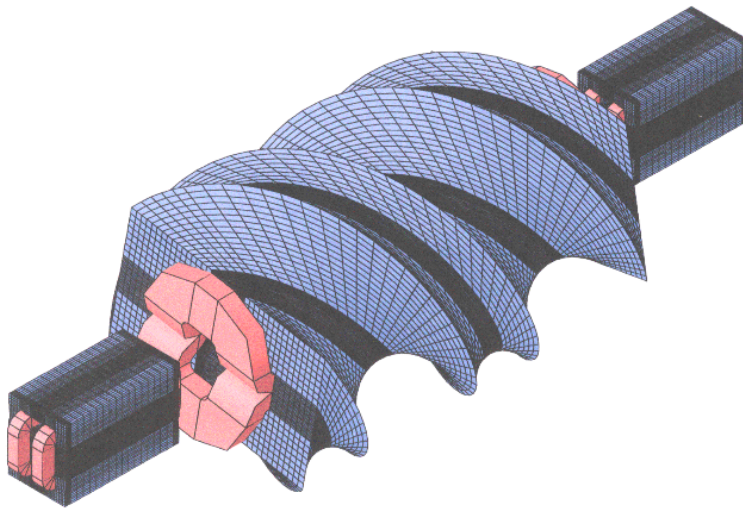Can be fit using a "bent box" geometry
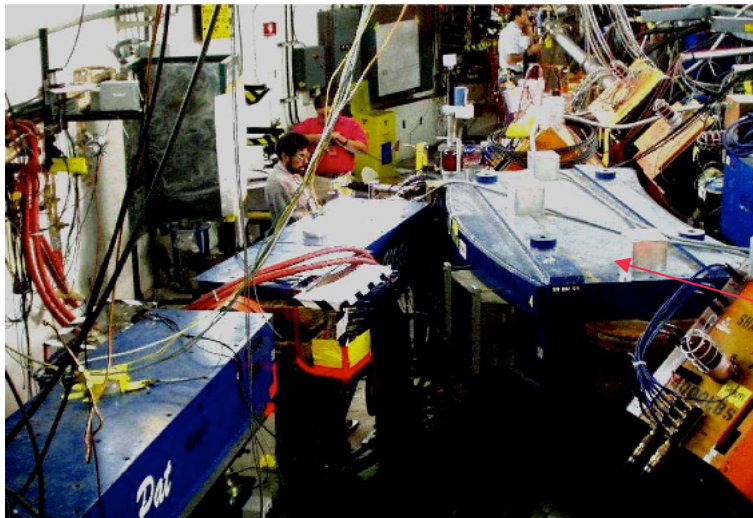
Proton Storage Ring (PSR) at Los Alamos LANSCE facility. Dipole on the right has a bending angle of 36 degrees, path length of 2.54948 m and sagitta of 23.83 cm.

General Surfaces: Helical Dipole

Proposed helical dipole design with oscillating aperture (helical fields serve to rotate spin polarization of the beam).

Design of the "Warm Snake" helical dipole appearing in the Alternating Gradient Synchroton (AGS) at Brookhaven National Laboratory.

General Surfaces: Bent Transport Line

The MECO Apparatus

Muon Stopping Target

Superconducting Transport Solenoid (2.5 T – 2.1 T)
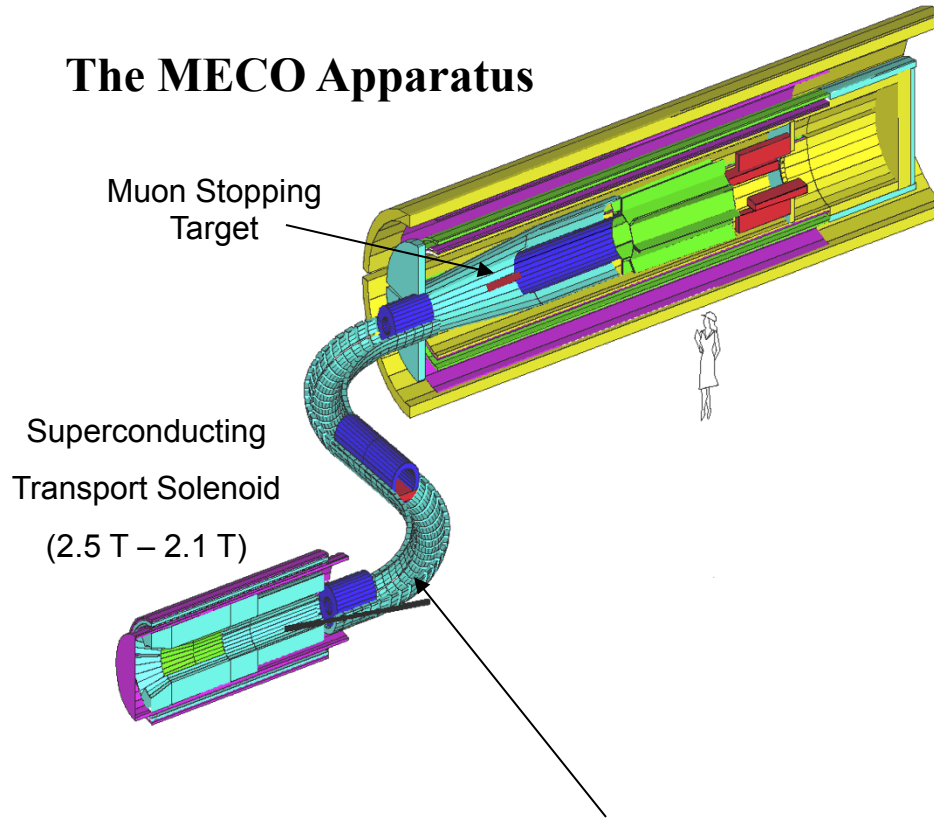
Proposed Muon-Electron Conversion (MECO) experiment at AGS in Brookhaven National Laboratory to search for lepton flavor violation. Abruptly cancelled August, 2005.

• Curved solenoid transport line eliminates transport of line-of-sight photons and neutrons.
• Curvature drift, collimators serve to momentum select beam.

General Surfaces

Using the Helmholtz theorem and results relating to Dirac monopoles, we may write the interior vector potential in terms of surface data in the form

$$A = A^n + A^t \text{ , where}$$

$$A^n(r) = \int_S [n(r') \cdot B(r')] G^n(r;r',m(r')) dS'$$

$$A^t(r) = \int_S \psi(r') G^t(r;r') dS' \text{ .}$$

The kernels are given by:

$$G^n(r;r',m) = \frac{m \times (r - r')}{4\pi |r - r'| \left[|r - r'| - m \cdot (r - r')\right]}$$ normal component

$$G^t(r;r') = \frac{n(r') \times (r - r')}{4\pi |r - r'|^3}$$ tangential components

where m is a unit vector pointing along some line that does not intersect the interior (a Dirac string), and n is the unit normal to the surface at r'.

The kernels G^n and G^t satisfy the properties:

- Analytic in the variables r at all points in the interior.

- $\nabla \times (\nabla \times G^t(r;r')) = \nabla \times (\nabla \times G^n(r;r',m)) = 0$ for all points r in the interior.

- $\nabla \cdot G^t(r;r') = \nabla \cdot G^n(r;r',m) = 0$ for all points r in the interior.

As a result, the vector potential A is guaranteed to satisfy Maxwell's equations $\nabla \times (\nabla \times A) = \nabla \times B = 0$ and the Coulomb gauge condition $\nabla \cdot A = 0$.

Given a point along the design orbit, we may construct a power series for A about r_d by integrating the surface data against the power series for the G's, term-by-term.

Each Taylor coefficient is obtained from a single surface integration.

This has been implemented numerically to compute coefficients a_l^w of the vector potential about any point on the design orbit.

Code accepts as input 3d data of the form $(\boldsymbol{B}, \psi)$ on a mesh and will produce as output:

1) Vector potential A at any interior point (gauge specified by orientation of strings)

2) Taylor coefficients of A about any design point through degree N

which in turn are used to compute…

3) Interior field B at any point

4) Taylor coefficients of B about any point   benchmark tools

5) $\nabla \cdot A, \quad \nabla \times A, \quad \nabla \cdot B, \quad \nabla \times B$

    as Taylor series through degree N-1
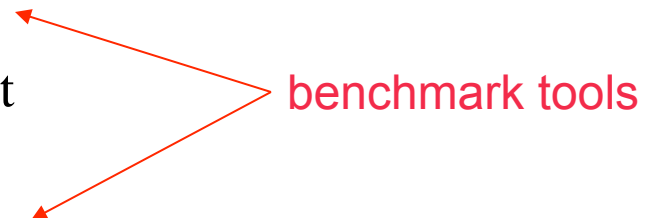
Code produces interior fits that satisfy Maxwell's equations exactly and $\nabla \cdot A = 0$ even if the required surface integrals are performed approximately.

Transfer maps are then computed from the Taylor expansion of $\boldsymbol{A}$ along the design orbit.

Benchmarks for various domains

straight box

sphere

torus

bent box
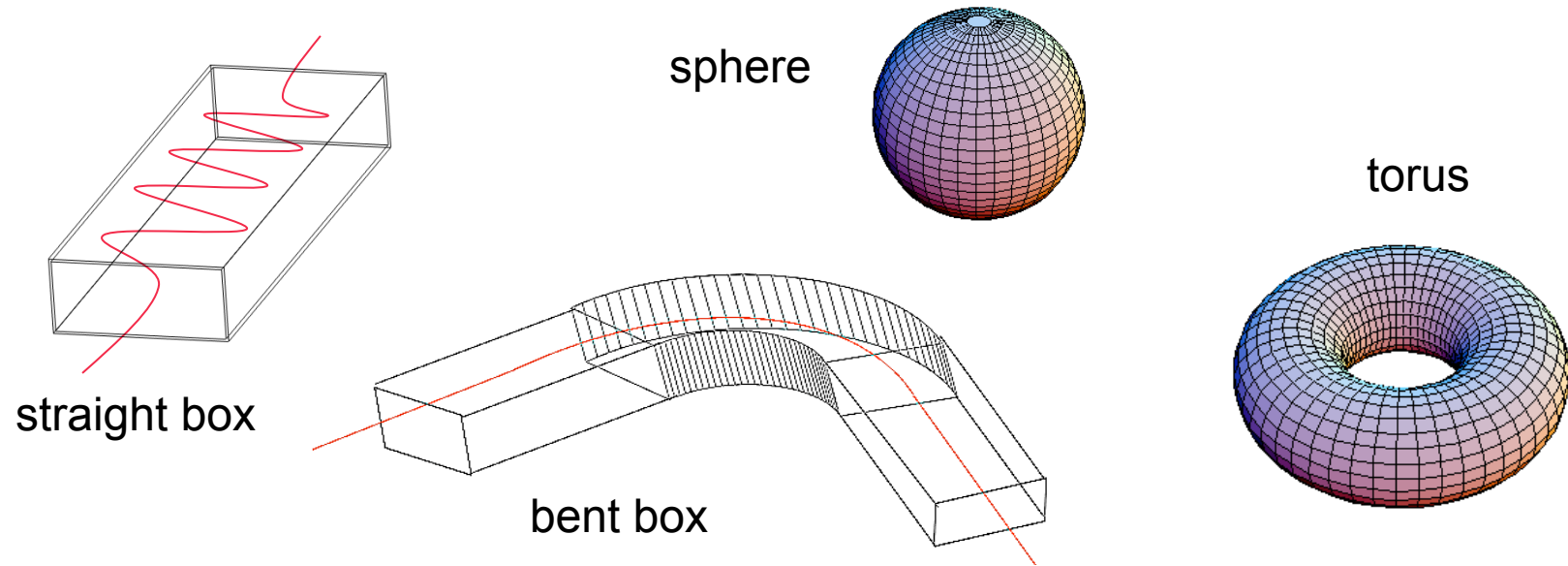
The procedure has been benchmarked for the above domains using arrays of magnetic monopoles to produce test fields. Power series for the components of B at a given point r_d are computed from the power series for A. These results can be compared to the known Taylor coefficients of the field. We find, using a surface fit that is accurate to 10^{-4}, that all computed coefficients are accurate to 10^{-6}.

Similarly, we verify that $\nabla \cdot B = 0$, $\nabla \times B = 0$, and $\nabla \cdot A = 0$ to machine precision.

Box Fit to ILC Wiggler Field

As an additional test, data provided by Cornell of the form (B_z, B_x, B_y, ψ) at grid points was fit onto the surface of a nearly-straight box filling the domain covered by the data. Box: 10 x 5 x 480cm Mesh: 0.4 x 0.2 x 0.2cm

Using this surface data, the power series for the vector potential was computed about several points in the interior. From this, the value of **B** was computed at various interior points and compared to the initial data.

interior points

Difference	(0.4, 0.2, 31.2) cm	(2, 2, 1) cm	(0, 1.4, 31.2) cm
Bx (G)	0.0417	0.187	0.230
By (G)	0.299	2.527	0.054
Bz (G)	0.161	0.626	0.916

Peak field=17kG   Largest error/peak ~ 10^{-4}

Properties of solution:

- Guaranteed to satisfy Maxwell's equations exactly.
- Sources of error are controlled: surface interpolation and multivariable integration--can be treated as error in the surface functions B_{normal} and ψ .
- Error is globally bounded.
- High-frequency random numerical errors on the surface are damped in the interior (smoothing).

Challenges:

Reduce runtime. Operation count $\sim LMNp$. Computation can be parallelized.

L - number of points evaluated along design orbit
M - number points on surface mesh
N - degree of coefficients required by Lie map
$p(N)$ - operations required by TPSA expansion of kernel

V. Conclusions -- What we did:

- Developed and implemented surface-fitting routines for domains of various geometry required for computing maps for general beamline elements.

- Involved developing routines to compute Mathieu functions, spline functions, and expansions of geometry-independent integration kernels.

- Studied error bounds and smoothing of numerical noise for these routines.

- Rewrote existing GENMAP routine for integrating map equations using truncated power-series algebra (TPSA) routines.

- Applied to compute maps for the prototype wiggler of the ILC damping rings.

- Ongoing applications to Brookhaven (NSLS-II) dipoles, LHC final-focus quadrupoles.

Future Applications to ILC Damping Ring Studies

- Characterize all beamline elements by realistic symplectic transfer maps in Lie form

$$M = \mathcal{R}_2 e^{:f_3:} e^{:f_4:} e^{:f_5:} e^{:f_6:} \ldots$$

- Potential to compute all single-particle properties of the DR from a single combined one-turn map, using only real field data for the entire ring.

- Includes all fringe-field effects on dynamic aperture, tunes, chromaticities, anharmonicities, linear and nonlinear lattice functions, etc.

- Can be used to check models of beamline elements, but use of models is no longer required.

- Could produce hybrid code using both Lie maps and PIC-computed space charge effects.